PHYSICAL REVIEW MATERIALS **3**, 085605 (2019)

Measurement of the stiffness of hard-sphere colloidal crystal-liquid interfaces

S. Z. van Loenen,[1,2] T. E. Kodger,[1,2] E. A. Padston,[2] S. Nawar,[2] P. Schall,[1] and F. Spaepen[2]
[1]*Van der Waals-Zeeman Institute, University of Amsterdam, Amsterdam 1098 XH, The Netherlands*
[2]*School of Engineering and Applied Sciences, Harvard University, Cambridge, Massachusetts 02138, USA*

(Received 1 April 2019; published 19 August 2019)

We investigated the stiffness of the interfaces between hard-sphere colloidal face-centered cubic crystals sedimented onto (100), (110), and (111) oriented templates and their equilibrium liquid with special attention to the in-plane anisotropy. The stiffness was determined from thermal fluctuations in the interface position imaged by confocal microscopy. The colloidal particles of diameter σ are nearly density-matched with the suspending fluid so that the amount of liquid above the interface was much greater than in an earlier similar hard-sphere colloid experiment. We find stiffness values of 0.47 k_BT/σ^2 for the (100) interface 0.53 k_BT/σ^2 for the (110) interface and 0.41 k_BT/σ^2 for the (111) interface. These values are generally closer to those found in computer simulations than to the earlier colloid results. No evidence was found however for the expected in-plane anisotropy of the (110) interface. This surprising finding confirms that of the earlier colloid work.

DOI: 10.1103/PhysRevMaterials.3.085605

I. INTRODUCTION

The interface between a crystal and its melt is of great interest in materials science. It presents fundamental physical questions, such as the spatial variation of long- and short-range order and of the thermodynamic potentials [1–3]. The interfacial free energy γ plays a key role in the kinetics of crystallization, both in the formation of the crystal nucleus [4] and the stability of the moving interface [5]. The value of the interfacial free energy depends on the orientation of the crystal face normal $\hat{\mathbf{n}}$. This anisotropy is important, for example for the equilibrium shape of small crystals in a melt, or for the formation of dendrites during solidification [6].

One way to study the interfacial free energy and its anisotropy, $\gamma(\hat{\mathbf{n}})$, is by the capillary fluctuation method (CPM) [7,8]. Thermal excitation causes an equilibrium interface to roughen: it fluctuates in time about its average position by $h(x, y, t)$, where x and y are the coordinates in the average interface plane. Fourier analysis of these deviations yields a power spectrum, which, upon time-averaging gives

$$\langle |h(\mathbf{q})|^2\rangle = \frac{k_BT}{\tilde{\gamma}(\hat{q})q^2}, \qquad (1)$$

where $\mathbf{q}$ is a vector parallel to the interface and $\tilde{\gamma} = \gamma + \frac{\partial^2\gamma}{\partial\theta^2}$ is the interface stiffness; θ is the angular variation of the interface normal in the direction of $\mathbf{q}$. The variation of $\tilde{\gamma}$ with direction in the plane, $\hat{\mathbf{q}}$, is described by a second rank tensor [9]. A polar plot of $[\tilde{\gamma}(\hat{\mathbf{q}})]^{-\frac{1}{2}}$ is therefore an ellipse, which must have the symmetry of the crystal face. In cubic systems, this means that for the (100) and (111) interfaces $\tilde{\gamma}$ must be isotropic in the plane. The (110) interface, however, is expected to be anisotropic, with the principal directions of $\tilde{\gamma}$ along [001] and [$\bar{1}$10].[1]

The stiffness of the crystal-liquid interface has been studied in computer simulations [8,10–12] and experimentally in colloidal systems [13–15]. The use of colloidal particles as a versatile model system for atomic solids has a long-standing history of providing invaluable insight into otherwise challenging phenomena to observe within atomic solids, e.g., crystallization [16], glassy dynamics [17], and grain boundaries [18]. The latter consist of dense suspensions of small particles (diameter $\sigma \approx 1$ μm) that can be tracked by confocal microscopy, which allows direct measurement of the fluctuating positions of the interface. For comparison of experiment and simulation, the hard-sphere system has the advantage that nearly the same potential can be used in the two approaches. Table I shows the results of hard-sphere simulations and experiments for face-centered cubic (FCC) crystal-liquid interfaces of highest symmetry.

Most striking about them is that all simulations [10–12] show a strong anisotropy of the (110) interface.[2] The colloid experiments of Ramsteiner *et al.* [14], on the other hand, showed surprising isotropy for the (110) interface.

---

[1] Through this paper, we utilize crystallographic notation for the face-centered cubic system. The conventional coordinate axes are parallel on the fourfold rotation axes, with length unit, at close packing, $a = \sigma\sqrt{2}$; $[hkl]$ represents a vector $\mathbf{r}_{hkl} = a(h, k, l)$; $\bar{h}$ means $-h$; and (hkl) represents an infinite set of parallel planes perpendicular to $\mathbf{r}_{hkl}$, evenly spaced by a^2/r_{hkl}. For a general treatment, see for example, Ref. [27]. The (100) and (111) planes have, respectively, four- and threefold rotational symmetry, and therefore have isotropic second-rank tensor properties [27,28]. The (110) planes have twofold rotational symmetry, which allows anisotropy.

[2] Reference [11] states that the stiffness for (110)[0$\bar{1}$0] is 0.41 $k_BT\sigma^{-2}$, which is why that value is listed in the (110)[001] column in Ref. [14]. The [1$\bar{1}$0] direction, does not lie in the (110) plane, and the statement in Ref. [11] is therefore most likely a misprint for (110)[1$\bar{1}$0], the direction discussed in the rest of their paper.

TABLE I. Calculated and measured values of the crystal-liquid interface stiffness $\tilde{\gamma}$ (in k_BT/σ^2) for the highest-symmetry orientations and directions of a hard-sphere FCC crystal. The last row is the areal density of the planes in closest-packed FCC, in atoms/σ^2.

(100)	(110)[$\bar{1}$10]	(110)[001]	(111)	Method	Ref.
0.55	0.49	0.71	0.80	MC	Mu *et al.* [12]
0.44(3)	0.42(3)	0.70(3)	0.67(4)	MD	Davidchack *et al.* [10]
0.43(1)	0.41(2)		0.74(3)	MD	Amini and Laird [11]
1.3(3)	1.0(2)	1.0(2)	(0.66)	silica colloids	Ramsteiner *et al.* [14]
0.47(3)	0.53(5)	0.53(5)	0.41(4)	FEMA-BMA colloids	This work
1.00	0.71	0.71	1.15	areal density	

Furthermore, their absolute values were significantly higher than those of the simulations.

The experiments of Ramsteiner *et al.* [14] were performed with silica spheres ($\sigma = 1.55\ \mu$m) in a water/DMSO suspending fluid. Because the density difference between particles and fluid is large ($\rho = 2$ g/cm^3 versus $\rho = 1.06$ g/cm^3, respectively), the gravitational length is small: $\frac{k_BT}{g\,\Delta\rho\, V_p} = 0.14\,\sigma$ (V_p: particle volume). As a result, the height of the liquid phase above the crystal after sedimentation is only a few particle diameters, which could have affected the structure and properties of the interface. We have therefore repeated these experiments in a colloidal system with a much greater gravitational length (1.7σ) to assess both the absolute values of the stiffnesses and the surprising finding of isotropy of the (110) interface.

II. EXPERIMENTS

We synthesized colloidal particles composed of a copolymer, formed from 2,2,2-trifluoroethyl methacrylate (FEMA, SynQuest Laboratories) and t-butyl methacrylate (tBMA, TCI America); their density ρ and refractive index n can be tuned by adjusting the monomer ratio such that a FEMA:tBMA ratio of 36:64 by volume resulted in $\rho = 1.202$ g/cm^3 and $n = 1.452$ [19]. By using formamide (FM) as the suspending fluid, the particles were refractive-index matched with the fluid and their density difference $\Delta\rho = 0.0727$ g/cm^3 was much smaller than that in the silica experiments ($\Delta\rho = 0.94$ g/cm^3) [14]. The particles have a diameter $\sigma = 1.55\,\mu$m and are suspended in a fluorescently dyed solution of 30 mM NaCl, formamide and rhodamine-B at a particle volume fraction of $\phi = 2\%$. The added salt screens the slightly negatively charged polymer brushes to obtain nearly hard-sphere behavior; the short ranged electro-steric repulsion results from an approximate 5–7-nm steric layer on the surface of each particle and a sufficiently screened electrostatic repulsion from the added salt, resulting in an estimated Debye screening length, $\kappa^{-1} = 1.5$ nm.

The copolymer particles were sedimented onto a 0.5 mm ×0.5 mm template that consists of holes etched in a glass cover slide in (100), (110), and (111) arrangements at nearest-neighbor distances of 1.64 μm. The holes accommodate the first layer of particles. Sedimentation produces horizontal (100), (110), and (111) FCC crystal-liquid interfaces [20–22]. To obtain nearly perfect (110) oriented crystals, it was necessary to deposit a few layers of particles onto the template by centrifugation of the sample chamber at 10g for 4 hours, after which additional particles were sedimented under regular gravity for at least another day. In all cases, planar, horizontal crystal-liquid interfaces between roughly 100-μm crystal and at least 40 μm of liquid were produced.

The samples were imaged from below with a Leica TCS SP5 through a 63× glycerol immersion objective. The microscope stage was leveled and the samples left on the microscope for at least a day before each measurement to minimize particle flow due to sample tilt. Individual particles were then imaged in volumes 102 μm × 102 μm in-plane and 60 μm in height centered around the interface. The resulting crystals

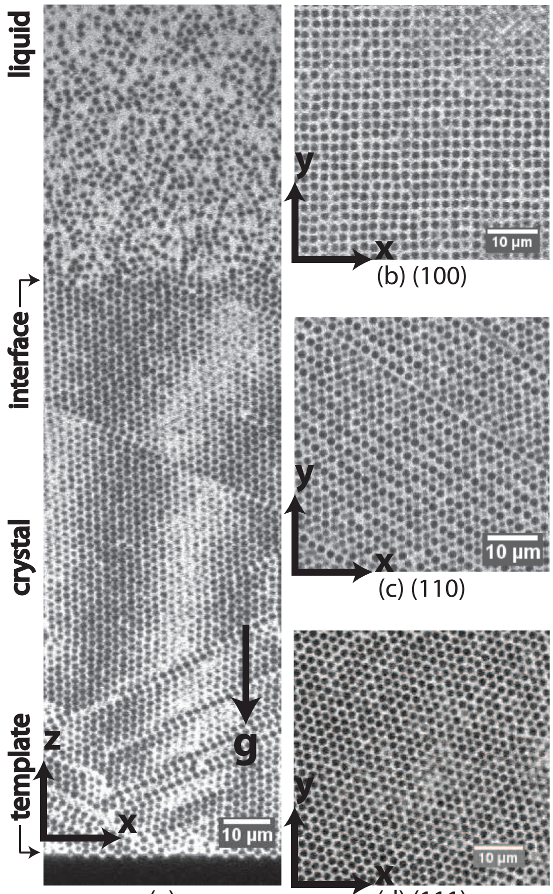

FIG. 1. (a) Vertical slice taken from the confocal image of a (110) crystal-liquid interface. The direction of gravity is marked. [(b)–(d)] Horizontal slices from the confocal images of (100) (b), (110) (c), and (111) (d) interfaces, The horizontal slices are taken ≈5 μm under the interface position. All images represent 1/4 of the total 2D image size.

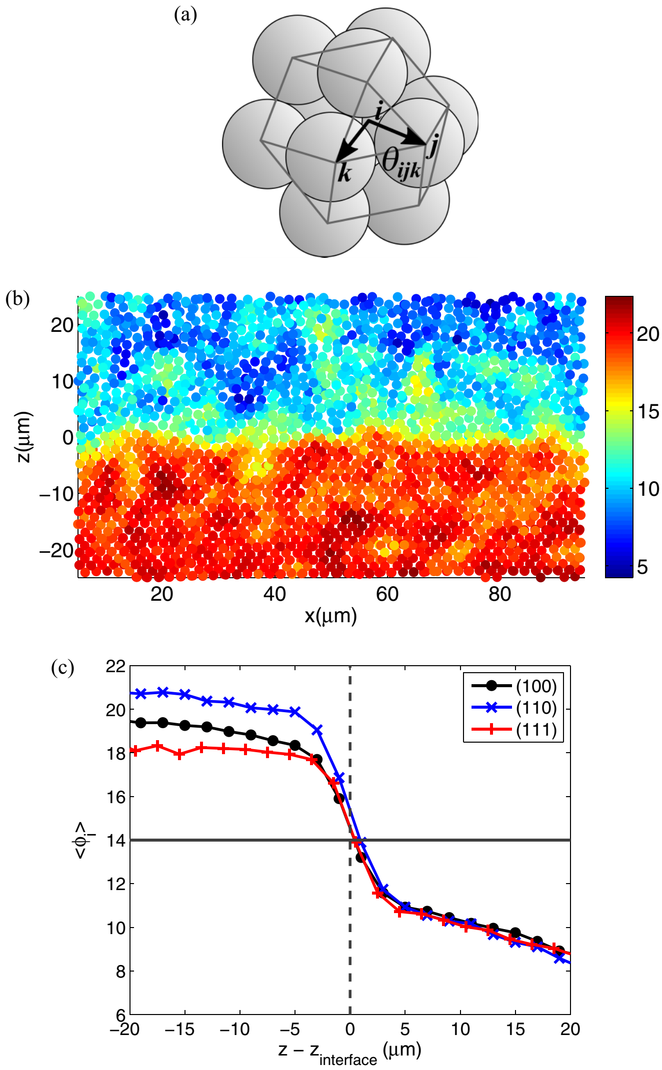

FIG. 2. (a) Schematic illustration of the bond angle θ_{ijk} of a particle in an FCC lattice. The order parameter, ϕ_i, is the number of angles with $\theta_{ijk} \approx 60^\circ$ or $\cos\theta_{ijk} = 0.5 \pm 0.2$. (b) Reconstruction of a vertical slice of a (100) crystal-liquid interface, where the color code indicates the value of the order parameter, ϕ_i, for each particle. (c) The average value of the order parameter $\langle\phi_i\rangle$ as function of height z for the (100), (110), and (111) interfaces. A bin size of $\Delta z = 3\ \mu$m was used to calculate the averages.

are of dimension over the total area of the template, thus the confocal microscope images capture only ∼4% of the total. The particle centers were located in three dimensions using standard particle tracking software [23,24]. For each orientation, the interface region was imaged every 6 minutes for at least 14 hours, resulting in 140–200 recordings.

III. RESULTS

Vertical and horizontal cross-sections through the colloidal crystal and liquid are shown in Fig. 1. Typically, the sedimented crystals reach a height greater than 100 μm as shown in Fig. 1(a), where the crystal-liquid interface is clearly visible. The crystals contain a few stacking faults, mostly in the lower part. Given that the stacking fault energy in hard-sphere systems is negligibly small, the small concentration of stacking faults is surprising, especially in the (111) orientation. Hydrodynamic effects probably play a role in favoring the FCC stacking. All data are therefore taken at interfaces well away from crystal defects.

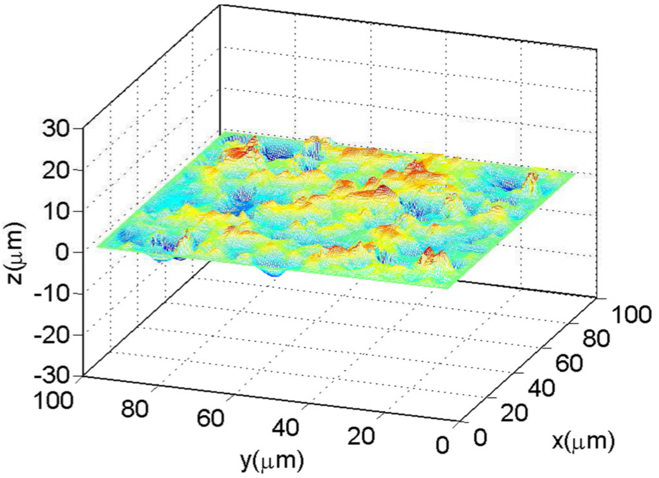

FIG. 3. Representation of the interpolated fluctuation heights of a (100) interface.

To locate the interface, we identify crystalline and liquid particles with a bond order parameter. We use the definition of Ramsteiner *et al.* [14], in which the order parameter, ϕ_i, of particle i is the number of bond angles θ_{ijk} between two nearest neighbours j, k of particle i that are close to 60° [Fig. 2(a)] ($\cos\theta_{ijk} = 0.5 \pm 0.2$). The nearest neighbors are defined as those closer than r_0, the first minimum of the pair correlation function of the crystal. This value varies slightly with crystal height and orientation; we therefore calculate it for each crystal orientation using a $20\ \mu\text{m} \times 20\ \mu\text{m} \times 20\ \mu\text{m}$ section of the sample, 5 μm below the crystal-liquid interface. For the (110) oriented crystal, for example, $r_0 = 2.25\ \mu$m. Each order parameter is then averaged over nearest neighbors to minimize artifacts due to thermal motion or crystal defects.

A representation of the smoothed order parameter distribution in a vertical section across the interface is shown in Fig. 2(b). The crystalline and fluid regions are clearly distinguishable. The average order parameter as a function of height is shown in Fig. 2(c). All samples show three regions: the crystal region with large order parameter values at low z (the order parameter for perfect FCC is 24), the liquid region with low order parameter values at high z, and the transition region near the interface. All samples show similar height-dependent order parameters in the liquid, but different values in the crystal region that depend on the crystal orientation. This indicates a variation in the quality of the crystals grown in the three orientations.

We determine the particles belonging to the interface by a method described by Mu *et al.* [12]. First, we consider all particles with bond order parameter smaller than a threshold ϕ_s to be part of the liquid. Then, for every remaining particle, we count the number Z_n of crystalline neighbors, and consider particles with Z_n smaller than a threshold Z_s to be part of the interface. Following Ramsteiner *et al.* [14], we restricted our choice to $Z_s = 9$ and $Z_s = 10$, and found that $Z_s = 9$

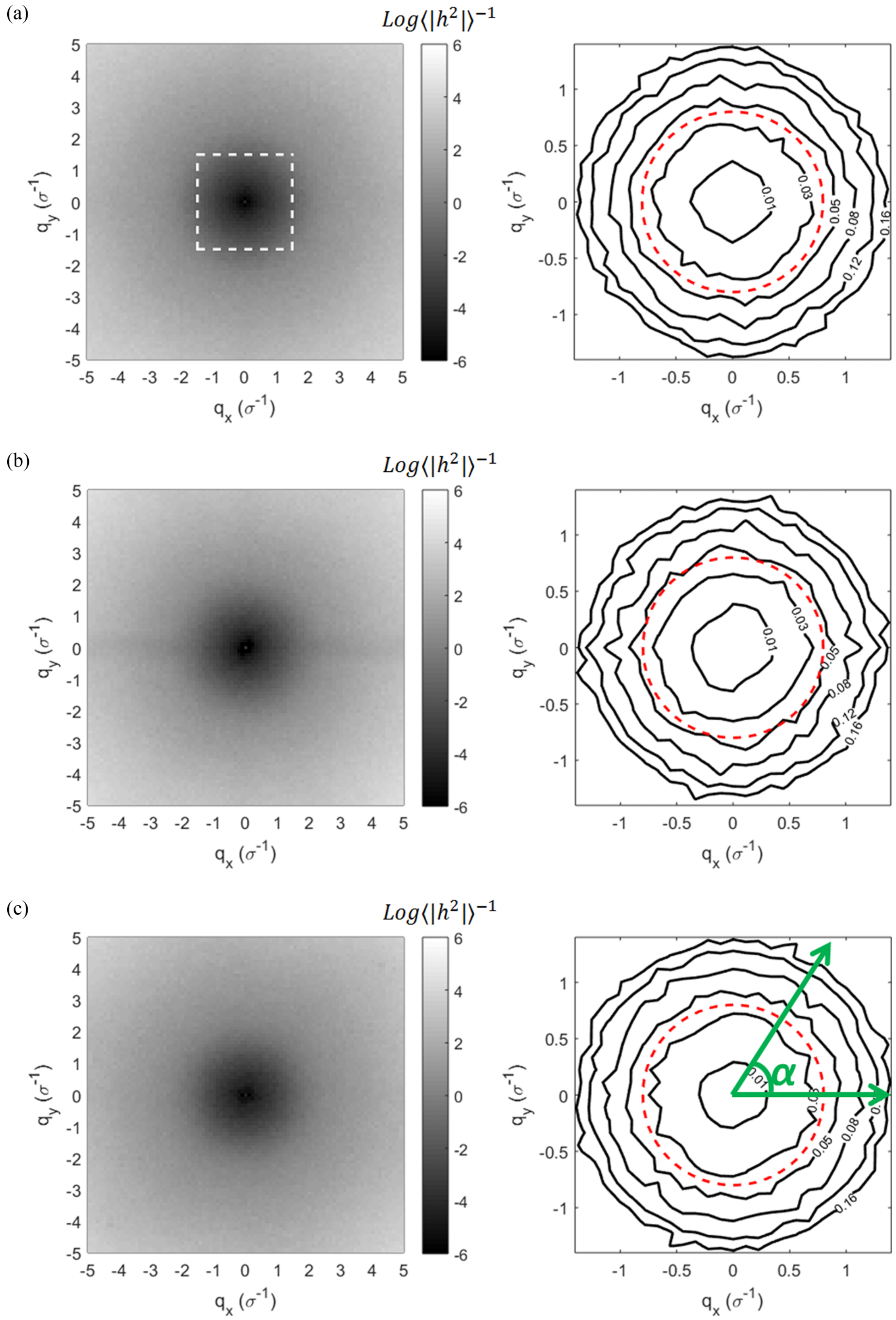

FIG. 4. [Left (L)] Logaritmic grayscale plot of the inverse averaged squared Fourier components of the (100) (a), (110) (b), and (111) (c) interfacial height profile. [Right (R)] Linear contour plots near the center of the gray-scale image for the (100), (110) and (111) interfaces. The center is marked by the white square in (a)-L. (c)-R shows a schematic representation of the angle α. The red circle serves as a guide to the eye.

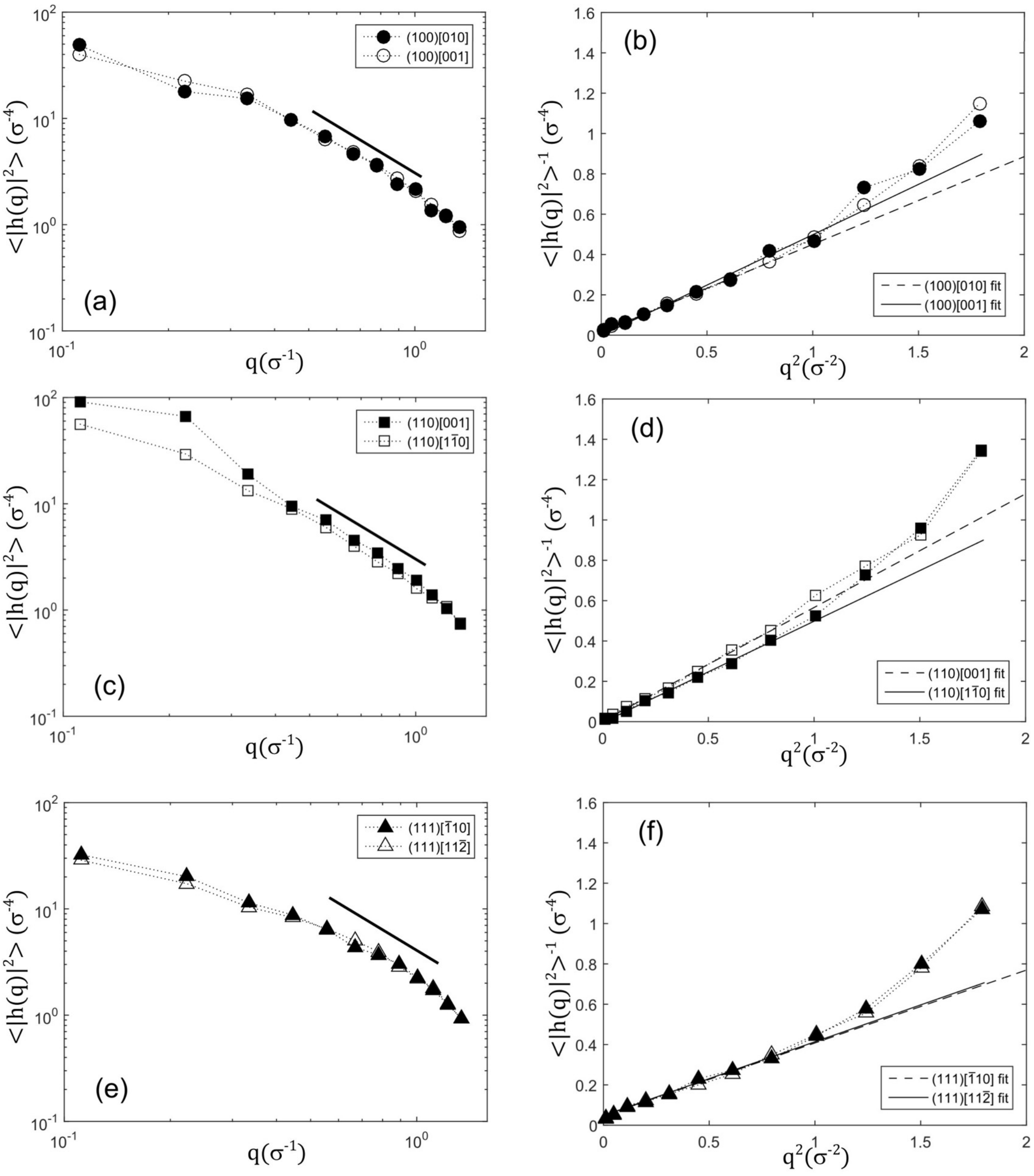

FIG. 5. Log-log plots of $\langle|h(q)|^2\rangle$ vs q for two high-symmetry directions in the (a) (100), (c) (110), and (e) (111) interface. The black line has a slope of -2. (b), (d) and (f) are the respective logarithmic-linear plots of $\langle|h(q)|^2\rangle^{-1}$ vs q^2. The solid and dotted lines are linear fits in the range $0.1\sigma^{-2} \leqslant q^2 \leqslant 0.8\sigma^{-2}$.

gave a the most consistent number of interface particles. As a final refinement, we required that every interface particle must have at least one other interface neighbor. In general, we found that a change in ϕ_s shifts the height of the interface, while retaining its overall shape. We chose $\phi_s = 14$, which locates the interface safely between crystal and liquid as shown in Fig. 2(c). A lower value of Z_s decreases the number of interface particles. We therefore use $\phi_s = 14$ and $Z_s = 9$ for all crystal orientations for consistency; deviations from these threshold values were extensively tested and did not alter the numerical conclusion of this work within experimental error.

We determined the height profile of the two-dimensional interface, $h(j, k)$, on a 0.5-μm spaced $L \times L$ square grid by interpolation of the heights of the identified interfacial particles. A reconstruction of the resulting interpolated interface is shown in Fig. 3, where the color indicates the vertical interface position. The reconstruction shows height fluctuations of several micrometers around an average flat horizontal interface. The Fourier coefficients of the height profile are [12,14]

$$h(\mathbf{q}) = h(m, n) = \frac{\Delta_{xy}^2}{\sqrt{A}}\left[\sum_{jk} h(j, k) e^{-i(\frac{2\pi}{L})mj} e^{-i(\frac{2\pi}{L})nk}\right], \quad (2)$$

where A is the total area in real space and L the number of grid points and $\Delta_{xy} = 0.5\ \mu\text{m} = 0.32\sigma$ is the interpolated spacing distance. Edge effects are minimized by imposing a tapered circular windowing mask with a diameter equal to the edge length of the interface; note, the taper employed is a

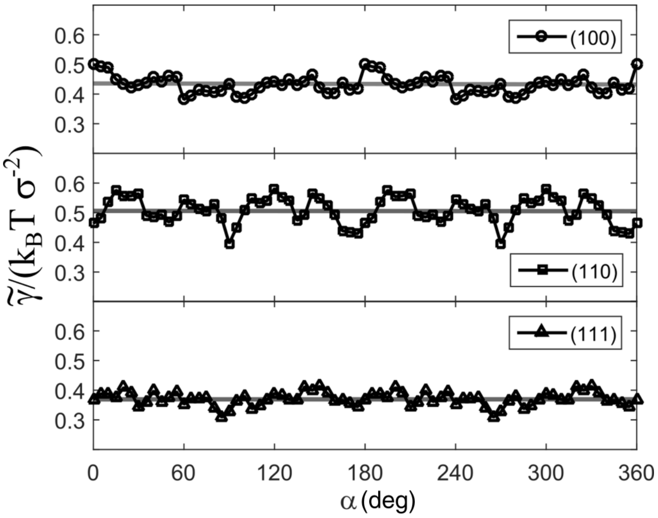

FIG. 6. Interfacial stiffness as a function of angle α in the plane for the (100), (110), and (111) interfaces. The horizontal lines indicate the average values, listed in Table I.

quarter-sine function of length 1 μm or approximately 5% of the total mask.

The squared Fourier coefficients were averaged over 140 recorded height profiles, and then along equivalent crystallographic orientations where appropriate. According to Eq. (1), the interface stiffness can be determined from the slope of the inverse squared Fourier coefficients, $\langle|h(\mathbf{q})|^2\rangle^{-1}$ with the square of the wave vector, q^2. Figure 4 shows two-dimensional plots of $\langle|h(\mathbf{q})|^2\rangle^{-1}$ for (100), (110), and (111) interfaces. Figures 5(a), 5(c), and 5(e) show log-log plots of $\langle|h(q)|^2\rangle$ as a function of q for three orientations and two high-symmetry directions in each plane. The dependence expected from Eq. (1) is indicated by the black line of slope -2. All data sets show good agreement with the expected dependence for q between 0.3 and $1\sigma^{-1}$; this range being bound in high-q by the particle size and low-q by the dimension of the confocal image.

To determine the stiffness, $\langle|h(q)|^2\rangle^{-1}$ was plotted as a function of q^2 in Figs. 5(b), 5(d), and 5(f). As in the logarithmic plots, we observe a linear relation for $q < 1.0\sigma^{-1}$, corresponding to wavelengths larger than the particle diameter. Significantly, the data go through the origin. In the silica experiments [14], there was an intercept at $q = 0$ equal to $\frac{g\Delta\rho\Delta\phi}{k_B T} = 0.57\sigma^{-4}$, where $\Delta\phi$ is the difference in packing fraction between the crystalline and liquid phases in equilibrium. The origin of this offset is the gravitational damping of the fluctuations due to the mass density difference between the two phases [25,26]. As expected, in the present experiments, where $\Delta\rho$ is much smaller, gravitational damping becomes negligible.

The interfacial stiffness was determined from the slope of a linear fit of $\langle|h(q)|^2\rangle^{-1}$ versus q^2 for $q < 1.0\sigma^{-1}$ along several directions at angles α [see Fig. 4(c)] in each of the planes. The results are shown in Fig. 6. The angular variation of the data for the (100) and (111) interfaces, which are isotropic, provides a measure of the experimental uncertainty, estimated at 10%. The angular variation for the (110) interface is slightly larger. The small dips observed at $\alpha = 0^\circ, 90^\circ, 180^\circ$, and 270° are transformation artifacts that align with the image axes whereas, significantly, the principal directions are along $\alpha = 75^\circ$ for [001] and $\alpha = 147^\circ$ for $[\bar{1}10]$ [see Fig. 1(c)]. The interfacial stiffness of the (110) interface, therefore does not show any measurable anisotropy. The average values of the interface stiffnesses are listed in Table I.

IV. DISCUSSION

Our stiffness values are significantly lower than those from the silica experiments [14] for all three orientations. The fractional decreases in stiffness are between 63% and 37%, which corresponds, according to Eq. (1), to fractional increases by half those values in the amplitudes of all the fluctuation modes, or approximately 20% to 30%. It is conceivable that the thinness of the liquid layer in the silica experiments suppressed the fluctuations compared to those into the fully formed liquid in the present experiments.

For the (100) interface and the $[\bar{1}10]$ direction on the (110) interface, the stiffness values we find are close to those of the three simulations. For the [001] direction on the (110) interface, however, there is a significant difference: we confirm the finding of the silica experiments that the (110) interfacial stiffness is isotropic, whereas the simulations show a clear anisotropy. The reason for this discrepancy is unclear. It is unlikely that a possible difference in the potentials plays a role, since that would lead to different overall stiffness values. Furthermore, the interaction distance of the colloids has been carefully minimized to resemble the hard-sphere potential as closely as possible. The sample size in the two approaches may play a role. In the colloid experiments, the interface is fully two-dimensional and extends over many hundreds of microns in all directions, even though only a smaller portion is imaged. For computational reasons, the simulations employ a quasi-one-dimensional method, in which the sample size perpendicular to the direction being studied is kept small. It is possible that this approach introduces or amplifies anisotropies. One indication, from an embedded-atom molecular dynamics simulation [8], is the anisotropy in the stiffness reported for the (100) interface (234 mJ/m^2 along [010]; 192 mJ/m^2 along [012]), which should be isotropic by symmetry.

Our value for the stiffness of the (111) interface is lower than that found in the silica experiments, but less so than for the other orientations. It was recognized the silica crystal contained many defects, right up to the interface. The resulting additional roughness may have lowered the measured stiffness for that orientation. The upper part of the corresponding crystal in the present experiments was defect-free, as was the interface. We therefore consider our value of the (111) stiffness to be reliable. It is surprising, then, that it is well below the values found in the simulations. The reason for this is not understood. It is interesting that our stiffness values correlate inversely with the areal density of the planes in the closest-packed crystal: 1.15 atoms/σ^2 for (111), 1 atom/σ^2 for (100), and 0.71 atoms/σ^2 for (110).

V. CONCLUSION

It has been worthwhile to repeat the measurements of the stiffness of high-symmetry crystal-liquid interfaces, made originally on hard-sphere silica colloids, with polymeric colloids that were more closely density-matched with the suspending fluid. The primary benefit was the creation of a tall, fully formed liquid phase above the interface, instead of a few micron thick liquid layer with the heavier particles. This yielded new, more reliable stiffness values that were systematically lower than the earlier ones. Nevertheless, a key observation of the silica experiments was confirmed: the stiffness of (110) interface was found to be isotropic in the plane, in contrast to the expectation of its crystallographic symmetry and to the computer simulations.

ACKNOWLEDGMENTS

This work was supported by the National Science Foundation under Contracts No. DMR-1206765 and No. DMR-1611089. P.S. acknowledges a VICI grant from the Netherlands Organization of Scientific Research (NWO). T.E.K. acknowledges a VENI grant from the Netherlands Organization of Scientific Research (NWO).

[1] D. P. Woodruff, *The Solid-Liquid Interface* (Cambridge Solid State Series, Cambridge University Press, 1973).

[2] J. M. Howe, *Interfaces in Materials* (Wiley, NY, 1997).

[3] F. Spaepen, Homogeneous nucleation and the temperature dependence of the crystal-melt interfacial tension, Solid State Phys. **47**, 1 (1994).

[4] K. F. Kelton and A. L. Greer, *Nucleation in Condensed Matter: Applications in Materials and Biology*, Pergamon Materials Series Vol. 15 (Elsevier, Amsterdam, 2010).

[5] M. Asta, C. Beckermann, A. Karma, W. Kurz, R. Napolitano, M. Plapp, G. Purdy, M. Rappaz, and R. Trivedi, Solidification microstructures and solid-state parallels: Recent developments, future directions, Acta Mater. **57**, 941 (2009).

[6] J. J. Hoyt, M. Asta, and A. Karma, Atomistic and continuum modeling of dendritic solidification, Mater. Sci. Eng. **R41**, 121 (2003).

[7] A. Karma, Fluctuations in solidification, Phys. Rev. E **48**, 3441 (1993).

[8] J. J. Hoyt, M. Asta, and A. Karma, Method for Computing the Anisotropy of the Solid-Liquid Interfacial Free Energy, Phys. Rev. Lett. **86**, 5530 (2001).

[9] D. Du, H. Zhang, and D. J. Srolovitz, Properties and determination of the interface stiffness, Acta Mater. **55**, 467 (2007).

[10] R. Davidchack, J. Morris, and B. Laird, The anisotropic hard-sphere crystal-melt interfacial free energy from fluctuations, J. Chem. Phys. **125**, 094710 (2006).

[11] M. Amini and B. B. Laird, Kinetic Coefficient for Hard-Sphere Crystal Growth from the Melt, Phys. Rev. Lett. **97**, 216102 (2006).

[12] Y. Mu, A. Houk, and X. Song, Anisotropic interfacial free energies of the hard-sphere crystal-melt interfaces, J. Phys. Chem. B **109**, 6500 (2005).

[13] J. Hernandez-Guzman and E. R. Weeks, The equilibrium intrinsic crystal-liquid interface of colloids, Proc. Natl. Acad. Sci. USA **106**, 15198 (2009).

[14] I. B. Ramsteiner, D. A. Weitz, and F. Spaepen, Stiffness of the crystal-liquid interface in a hard-sphere colloidal system measured from capillary fluctuations, Phys. Rev. E **82**, 041603 (2010).

[15] V. D. Nguyen, M. T. Dang, B. Weber, Z. Hu, and P. Schall, Visualizing the structural solid-liquid transition at colloidal crystal/fluid interfaces, Adv. Mater. **23**, 2716 (2011).

[16] P. N. Pusey and W. van Megen, Phase behavior of concentrated suspensions of nearly hard colloidal spheres, Nature (London) **320**, 340 (1986).

[17] E. R. Weeks, Three-dimensional direct imaging of structural relaxation near the colloidal glass transition, Science **287**, 627 (2000).

[18] T. O. E. Skinner, D. G. A. L. Aarts, and R. P. A. Dullens, Grain-Boundary Fluctuations in Two-Dimensional Colloidal Crystals, Phys. Rev. Lett. **105**, 168301 (2010).

[19] T. E. Kodger, R. E. Guerra, and J. Sprakel, Precise colloids with tunable interactions for confocal microscopy, Sci. Rep. **5**, 14635 (2015).

[20] A. van Blaaderen, R. Ruel, and P. Wiltzius, Template-directed colloidal crystallization, Nature (London) **385**, 321 (1997).

[21] I. B. Ramsteiner, K. E. Jensen, D. A. Weitz, and F. Spaepen, Experimental observation of the crystallization of hard-sphere colloidal particles by sedimentation onto flat and patterned surfaces, Phys. Rev. E **79**, 011403 (2009).

[22] K. E. Jensen, D. Pennachio, D. Recht, D. A. Weitz, and F. Spaepen, Rapid growth of large, defect-free colloidal crystals, Soft Matter **9**, 320 (2013).

[23] Y. Gao and M. L. Kilfoil, Accurate detection and complete tracking of large populations of features in three dimensions, Opt. Express **17**, 4685 (2009).

[24] K. E. Jensen and N. Nakamura, Note: An iterative algorithm to improve colloidal particle locating, Rev. Sci. Instrum. **87**, 066103 (2016).

[25] D. G. A. L. Aarts, M. Schmidt, H. N. W. Lekkerkerker, and K. Mecke, Microscopy on thermal capillary waves in demixed colloid-polymer systems, Adv. Solid State Phys. **45**, 15 (2005).

[26] D. Bedeaux and J. D. Weeks, Correlation functions in the capillary wave model of the liquid-vapor interface, J. Chem. Phys. **82**, 972 (1985).

[27] M. J. Buerger and Dan McLachlan, Elementary crystallography, Am. J. Phys. **25**, 272 (1957).

[28] J. F. Nye, *Physical Properties of Crystals* (Oxford University Press, Oxford, 1985).